Euler Flow Analysis of Turbine Powered Simulator and Fanjet Engine

Naoki Hirose* and Keisuke Asai†

National Aerospace Laboratory, Tokyo, Japan

and

Katuya Ikawa‡ and Ryuma Kawamura§

Nihon University, Funabashi, Japan

An Euler flow analysis of turbine powered simulator (TPS) and fanjet engine was made utilizing MacCormack's finite volume scheme. TPS simulation computations for an axisymmetric geometry were compared with experimental data obtained in the National Aerospace Laboratory transonic wind tunnel. The pressure distributions on the inlet cowl and corejet cowl surfaces showed excellent agreement. The effect of differences in engine conditions of corejet temperature and mass flux between the TPS flow and a real fanjet engine was analyzed with the computations. The results showed no significant differences in the external flowfield surrounding the exhaust jet plume. A three-dimensional analysis showed the effects of angle of attack on the inlet flowfield and exhaust jet plume.

Introduction

INLET aerodynamics and flow analysis around a fanjet engine are important in the design of engine nacelles because the fan is large in current engines, and knowledge of the detailed flowfield is required. The interaction of engine flow with the wing is also significant to avoid deterioration of the aerodynamic characteristics of the wing. Flow-through nacelle and ejector nacelle models have been used in the past in wind tunnel experiments of wing-body configuration with engines. Experimental analyses have been reported in the literature, e.g., Bagley and Kurn,[1] Langley,[2] and Crook.[3]

The turbine powered simulator (TPS) is considered a more accurate fanjet engine nacelle model in the wind tunnel because its operation is quite similar to a real fanjet engine except that the corejet exhaust gas is the air-turbine working gas rather than the products of combustion. During the development of the National Aerospace Laboratory (NAL) experimental STOL aircraft ASKA, which used upper surface blowing (USB) as a high lift device, a transonic wind tunnel testing technique utilizing the TPS was developed by Asai et al.[4] A preliminary axisymmetric nacelle configuration with the TPS was tested in the NAL 2 m × 2 m transonic wind tunnel to establish the TPS operational procedure[5,6] before the ASKA model was tested.

Although the TPS is the best simulation device used in the wind tunnel, there exist two items different from a real fanjet engine. The first is that the corejet is cold in the TPS and hot in the real engine. The second item is that the relation of mass flow ratio (*MFR*) and bypass ratio (*BR*) is different. In the TPS, all the inlet mass flow becomes the fanjet mass flow. The air-turbine working gas supplied from outside of the wind tunnel constitutes the corejet mass flow. In the real engine, the inlet mass flow is divided into the fanjet mass flow and corejet

mass flow. The effect of these differences on the flowfield is sought in the present paper.

Recent developments in computational fluid dynamics (CFD) enable analysis of this type of flowfield. Application of CFD to inlet aerodynamics can be found in the literature. Potential analyses, for example, were given by Arlinger,[7] Caughey and Jameson,[8] Chen and Caughey,[9,10] Reyhner,[11] Vadyak and Atta,[12] Nakamura,[13] Peace,[14] and Morice.[15] Euler analyses, which are better for strong shock waves, were made by Deese and Agarwal[16] and Chen et al.[17,18] The Navier-Stokes approach was tried by Nakahashi and Obayashi.[19] These works can be classified in the order of flow complexity. References 7, 8, and 9 treat axisymmetric inlet flow; Refs. 10, 11, 14, and 17 treat three-dimensional flow past an axisymmetric inlet; Refs. 12, 13 and 19 treat three-dimensional flow past a nonaxisymmetric inlet; and Refs. 15, 16, and 18 deal with a three-dimensional fanjet engine. Rubbert[20] emphasizes CFD's important role on nacelle design by referring to the actual design for a Boeing 737-300. Even though a simple potential analysis is applied to this case, it demonstrates CFD's effectiveness very well.

The exhaust jet flowfield and its interaction with the rear body also attract experimental and computational research because of the concern with the accurate estimation of the base drag and the jet thrust. Surveys of the research in this field were given by Bowers and Laughrey[21] and Putnam and Bissinger.[22] Peery and Forester[23] analyzed an axisymmetric fanjet nozzle with the Euler equations and Deiwert and Rothmond[24] treated three-dimensional flow of a single jet nozzle in a supersonic stream using the Navier-Stokes equations.

Consideration of the exhaust jet plume in the inlet aerodynamics adds complexity to the analysis and requires more computing resources. Flow around a fanjet engine is quite complicated with both fanjet and corejet exhaust plumes. However, both the inlet flow and exhaust plume flows must be considered to analyze engine nacelle aerodynamics precisely because they are closely coupled. A potential analysis does not provide appropriate clues to investigate this flowfield because the shear layer between the jet plume and mainstream flow must be replaced with an assumed vortex sheet. A Navier-Stokes analysis may provide the most detailed flowfield if fine enough grid resolution and an appropriate turbulence model are used to quantitatively analyze the high Reynolds number jet flowfield. Otherwise, a Navier-Stokes analysis only consumes a large amount of computing time without obtaining any significant result compared with an Euler analysis.

*Branch Chief, Aircraft Aerodynamics Division. Associate Fellow AIAA.

†Research Scientist, Aircraft Aerodynamics Division. Member AIAA.

‡Graduate Student; currently UNISYS Japan.

§Professor, Department of Aerospace Engineering (retired).

Therefore, an Euler analysis has been applied in the past with good reason. An Euler code can predict a more accurate shock wave strength and location in the inlet region compared with a potential code. An Euler code does not fail until the freestream Mach number becomes close to unity or the angle of attack becomes large enough so that viscous effects such as shock-induced separation become significant. In the region of the afterbody where interactions take place among the mainstream, fanjet and corejet, fundamental features of the flowfield such as the appearance of shock waves and expansion waves and reflections and deflections at the shear layers are inviscid phenomena and should be captured in the Euler analysis. Viscous effects are also less significant in high Reynolds number flows. Euler treatment of complicated flowfields similar to this were already made by the first author two decades ago and proved to be effective.[25] Euler analysis of the entire fanjet engine nacelle aerodynamics will provide a new approach to the problem. Such analysis has not yet been investigated enough to the authors' knowledge.

In the present paper, a three-dimensional Euler flow analysis is given for an axisymmetric TPS and fanjet engine geometry utilizing MacCormack's scheme in finite volume form. Axisymmetric flow cases for TPS simulation are compared with wind tunnel data. The differences between the TPS and real engine are analyzed simulating the respective engine conditions. Three-dimensional flow computations are made for real engine conditions. Angle of attack effects on the inlet flow and exhaust jet plume are analyzed.

Mesh Generation for Fanjet Engine

Geometric Configuration

The nacelle geometry and the computational mesh in the symmetry plane are shown in Fig. 1. This is an axisymmetric nacelle model, which is the same as that used in a preliminary TPS experimental investigation.[6] The model houses a Tech Development Inc. 1079A air-turbine simulator. The profile of the fan cowl was designed so that the flow is smooth over the spinner and fan hub. The outer fan cowl surface is part of an ellipse, and the leading edge regions is modified to fair smoothly with the inner surface. Both the fanjet and corejet nozzles are convergent to their respective exits. The model has a fan cowl chord of 215 mm and highlight radius of 45 mm. The details of the model are given in Ref. 6. Hereafter in the paper, dimensions are normalized by the fan cowl chord.

Computational Region and Mesh Generation

The computational region in the symmetry plane is shown in Fig. 2. The region extends from $x = -3$ to $+3$ in the flow direction and from the axis to $r = 2$ in the radial direction. The highlight is located at $x = 0$. The computational mesh consists of three regions: the fan cowl mainflow region A, the fanjet region B, and the corejet region C. The body-fitted nonorthogonal mesh coordinates (ξ, η) are defined with ξ along the fan cowl surface in the stream direction. In region A, a C-type mesh extending from the inlet fan face to the downstream

boundary is constructed by the elliptic equation method. Several η lines are constructed geometrically near the surface to maintain orthogonality to the body surface. The distribution in the η direction is clustered. Regions B and C use simple H-type meshes. The mesh is clustered along the "wake" boundaries connecting adjacent regions in order to capture the physical jet slip sheet, which may exist along them. A solution-adaptive grid was not applied, however, and the mesh is fixed in space in the present investigation.

For the three-dimensional analysis, the mesh in the symmetry plane was rotated 180 deg around the x axis. The major boundary surfaces: spinner, fan face, fan cowl, fanjet inner cowl, fanjet exit, corejet outer cowl, corejet inner cowl, corejet exit, and corejet spinner are shown in Fig. 1. Finite volume integration is done for each cell consisting of grid points of the mesh with cylindrical surfaces normal to η.

The axisymmetric fine mesh contains 122×24 cells in region A, 64×12 cells in region B, and 62×12 cells in regions C. Total cell number is halved in each direction in the coarse mesh analysis. The circumferential direction ξ was divided into 8 cells on one side of the symmetry plane in both the coarse and fine meshes.

Numerical Procedure

Governing Equations

The Euler equations written in integral form for cylindrical coordinates are

$$\int_V \frac{\partial}{\partial t} u \, dV + \int_S Q \cdot n \, ds + \int_V \frac{E}{r} \, dV = 0 \qquad (1)$$

where

$$U = \begin{bmatrix} \rho \\ \rho q_x \\ \rho q_r \\ \rho q_\theta \\ e \end{bmatrix}, \quad Q = \begin{bmatrix} \rho q \\ \rho q_x q + pj \\ \rho q_r q + pk \\ \rho q_\theta q + pl \\ (e+p)q \end{bmatrix}, \quad E = \begin{bmatrix} 0 \\ 0 \\ -\rho q_\theta^2 - p \\ \rho q_r q_\theta \\ 0 \end{bmatrix}$$

$$q = q_x j + q_r k + q_\theta l \qquad (2)$$

The notation is standard. The column vector U consists of density, axial, radial, and circumferential momentums and total energy per unit volume; q is velocity with respective components, q_x, q_r and q_θ; j, k, and l are unit vectors; p is pressure; Q is flux vector; and E is source term due to the cylindrical coordinates. Air is assumed as the corejet gas as well as the mainflow gas and is considered perfect.

Numerical Scheme

There is a wide variety of Euler schemes. Explicit schemes such as the Runge-Kutta and total variation diminishing (TVD) schemes are gaining popularity over implicit schemes because of their suitability to supercomputers. The MacCormack's scheme is a well-known explicit scheme. Coding is easy and validity is established. Furthermore, the extension to the contemporary TVD version can be easily incorporated as
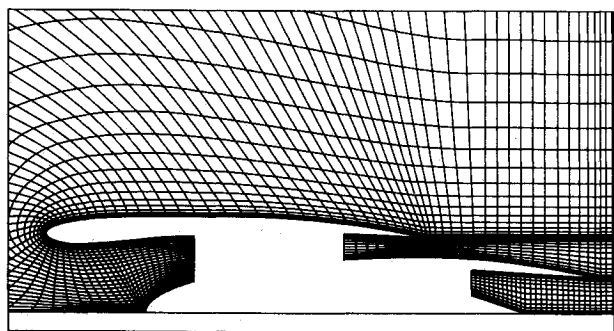

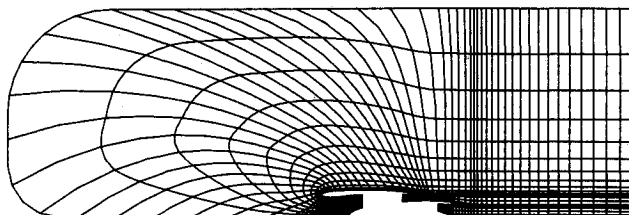
Fig. 1 Nacelle geometry and computational mesh.

Fig. 2 Computational region in symmetry plane.

shown by Yee and Shin[26] to obtain high resolution of shock waves. Extension to the Navier-Stokes equations can be made easily.

In the present analysis, the explicit second-order accurate MacCormack's scheme in finite volume form was applied to Eq. (1).[27,28] As addition of the TVD terms is expensive in using computing resources, it was not adopted here. The scheme in time-splitting form for the curvilinear coordinates (ξ, η, ζ) is described as

$$U^{n+1} = L_\zeta(\Delta t/2) \cdot L_\eta(\Delta t/2) \cdot L_\xi(\Delta t) \cdot L_\eta(\Delta t/2)$$

$$\cdot L_\zeta(\Delta t/2) U^n \tag{3}$$

For the axisymmetric computation, L_ζ is omitted. A conventional third-order fourth derivative dissipation term was added for stability. A local time step method is applied to obtain rapid convergence to the steady solution. The present MacCormack's finite volume method (FVM) scheme has been successfully applied to various flow problems by the present authors. Code validation was made and it proved to be excellent.[29,30] The details of the scheme may be found in the literature.

Boundary Conditions

Boundary conditions for the respective boundaries are given as follows.

Natural Boundary Conditions

At the upstream and side boundaries, the far-field boundary conditions are based on the theory of characteristics for locally one-dimensional inviscid flow.[31] For subsonic inflow, freestream Riemann invariant R_∞, tangential velocity components and entropy, and outgoing boundary Riemann invariant R_B extrapolated from inside the computational region give the set of variables required. A similar procedure is applied at the outflow boundary.

At the downstream boundary, which is located far behind the model, zeroth-order extrapolation in the ξ direction was applied for the entire downstream boundary including the supersonic jet plume and subsonic mainstream region. Riemann boundary condition may give better results where subsonic outflow exists. The extrapolation is justified for a supersonic jet.

At the body surface, a tangential slip flow condition was enforced. A symmetric boundary condition was applied at the symmetry plane. No mass flux exists at the axial boundary because the cell surface is reduced to zero in a finite volume approach.

At the wake boundaries, which connect adjoining computational regions, flow is physically continuous and, therefore, the cell variables are transferred to the corresponding boundary cell in each computational region.

Engine Face Boundary Conditions

Boundary conditions at the fan face of the inlet, fanjet exit, and corejet exit boundaries should be determined by the engine conditions or TPS operational status. Physically exact boundary conditions, however, are very complicated and difficult to specify. For example, the fan blades are rotating at the fan face boundary, and the boundary condition will be given as the three-dimensional time-dependent flowfield, which must be solved as the fan blade flow problem. Instead simplified model boundary conditions are applied by various authors; the reader is referred to Chen.[17] The simplified boundary condition is not unique, and several options are possible. At the fan face boundary of the inlet, only one variable such as mass flux, pressure, or velocity may be specified while the rest are obtained from the solution.

In the present analysis, the mass flow ratio of the air-intake MFR is specified. Mass flux per cross-sectional area at the fan face MF is given as

$$MF \equiv (\rho q)_{fan} = \rho_\infty \, q_\infty (A_{HL}/A_{fan}) MFR \tag{4}$$

where A_{HL} is the cross-sectional area at the highlight; A_{fan} is the fan area; and MFR is defined as A_∞/A_{HL}, where A_∞ is the cross-sectional area of inflow.

It is assumed that mass flux is radially uniform and velocity vector direction is linearly distributed from parallel to the spinner to parallel to fan cowl inner surface. Density and the circumferential velocity component are extrapolated from the flowfield. Pressure and energy are given using the adiabatic Bernoulli equation. Then all the variables at the fan face boundary required in the computation are determined as in Ref. 32.

At the jet exit boundaries, boundary conditions similar to those described above are specified using total pressure ratio and total temperature ratio of the exhaust jet MFR and bypass ratio BR. These values are obtained from experiment or computed by the engine thermocycle.

For example, at the fanjet exit boundary of the TPS simulation in which case all intake mass flux becomes fanjet mass flux, total density, ρ_{0F} and exhaust jet mass flux are given as

$$\rho_{0F} = \rho_{0\infty} \cdot FPR/FTR$$

$$(\rho q_x)_F = MF \cdot A_{fan}/A_{FEX} \tag{5a}$$

where FPR and FTR are total pressure ration and total temperature ratio of fanjet, respectively. A_{FEX} is the cross-sectional area of the fanjet exit. At corejet exit boundary, these are similarly given as

$$\rho_{0C} = \rho_{0\infty} \cdot CPR/CTR$$

$$(\rho q_x)_C = MF \cdot A_{fan}/A_{CEX}/BR \tag{5b}$$

where CPR and CTR are total pressure ratio and total temperature ratio of corejet, respectively. A_{CEX} is the cross-sectional area of the corejet exit. The other variables are derived similarly to those at fan face.

In the real engine simulation, inlet mass flux is divided into fanjet and corejet flow in proportion to the bypass ratio BR. Fuel added to the corejet flow can be neglected because the fuel to air ratio is at most ≈ 0.02. Then the mass fluxes at the fanjet and corejet exits are given as

$$(\rho q_x)_F = MF \cdot A_{fan}/A_{FEX} \cdot BR/(1+BR)$$

$$(\rho q_x)_C = MF \cdot A_{fan}/A_{CEX}/(1+BR) \tag{6}$$

The other variables are given as before.

Jet Starting Conditions

In some cases where the Mach number is high and MFR is large, the exhaust jet chokes in the nozzle duct when impulsive start conditions are enforced because the mass flux is fixed in the analysis. To correct this situation, the initial distribution of flow in the jet exhaust stream (regions B and C) was given as follows: 1) jet mass flux is reduced to one half that of the specified MFR or 2) jet exit Mach numbers M_{JF} and M_{JC} are specified to give p_J and ρ_J. The flow is eventually established without choking when these initial distributions are given. The boundary conditions during the iteration are given as specified previously.

Experiment

The experimental investigation has been reported in Refs. 5 and 6, and the details will not be given here. Pressure distributions on the fan cowl and core cowl surfaces and total pressure and total temperature distributions in the fanjet and corejet ducts were measured at zero incidence. Mach number M_∞ ranged from 0 to 0.8 and turbine revolution rate from windmill to maximum speed. Angle of attack effects were not investigated because of mechanical restriction on model installation in the wind tunnel.

Table 1   Engine operating conditions for axisymmetric flow cases

Case number	Mach number M_∞	Engine operating conditions					
		MFR	BR	FPR	CPR	FTR	CTR
1	0.6	0.30760	7.95	0.95044	0.78890	1.01150	1.00290
2	0.6	0.42451	3.03	1.08783	0.83703	1.03082	0.75329
3	0.6	0.49609	2.49	1.20517	0.88347	1.06338	0.67204
4	0.6	0.56483	1.70	1.35429	1.04704	1.10580	0.61826
5	0.6	0.59901	1.40	1.44358	1.21166	1.13226	0.61072
6	0.6	0.61598	1.42	1.48484	1.27665	1.14345	0.61033
13	0.8	0.31678	9.51	0.92978	0.68668	1.01198	0.99310
14	0.8	0.38763	3.24	1.05952	0.71701	1.03535	0.75125
15	0.8	0.44279	2.42	1.18190	0.78608	1.06662	0.66827
16	0.8	0.49730	1.82	1.34280	0.92126	1.10861	0.61185
17	0.8	0.52324	1.57	1.43035	1.12451	1.13299	0.60995
18	0.8	0.51739	1.20	1.46005	1.33113	1.14628	0.59441
21	0.8	0.7	2.5	4.0	4.0	3.0	5.0
22	0.8	0.52324	4.01	1.43035	1.12451	1.13299	4.0
23	0.8	0.645	4.01	1.43035	1.12451	1.13299	4.0

Computational Results and Discussion

Axisymmetric Flow of Turbine Powered Simulator Simulation

The code validity was checked first for the axisymmetric flow problem before comparison with the experiment was made. Comparison of computed flowfields with coarse and fine meshes showed agreement of results such as the surface pressure distribution. The resolution of shock waves was better in the fine mesh analysis. It was confirmed that the local time step method gave faster convergence with the same converged solution.

The axisymmetric flow of TPS simulation in a powered nacelle condition was analyzed using a fine mesh and physical time step method, and the computed results were compared with experimental data. Computations were made at flow Mach number $M_\infty = 0.6$, 0.7, and 0.8; from a windmill condi-

tion to a maximum rotation condition, which corresponds to a MFR of about 0.3 to 0.6. The engine conditions: mass flow ratio MFR, bypass ratio BR, fanjet total pressure ratio FPR, total temperature ratio FTR, corejet total pressure ratio CPR, and total temperature ratio CTR were taken from the experimental data. Table 1 shows a partial list of engine operating conditions for computed cases.

The computed surface pressure distributions on the fan cowl and core cowl surfaces were compared with the experimental distributions. For subcritical flow $M = 0.6$, excellent agreement was obtained for the MFR range computed. At higher Mach numbers, the agreement was again excellent, including the shock wave location and strength on the outer surface of the fan cowl. The pressure distribution along the fan cowl inner surface also agrees with the experiment. Figure 3 compares surface pressure distributions on the fan cowl and core cowl surfaces at MFR = 0.31678 (windmill) and 0.52324 (maximum) for $M_\infty = 0.8$. The experimental data denoted by the symbols agree with the computed results shown by the solid line. Figures 4 shows Mach number contours around the inlet and exhaust jet regions at the maximum MFR = 0.52324.

The computed results showed the effects varying MFR. At $M_\infty = 0.6$, a very narrow supercritical region of suction peak exists when MFR is less than 0.50. The shock wave is not clearly defined because of inadequate mesh resolution. The
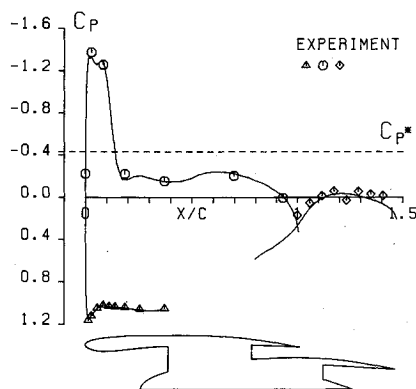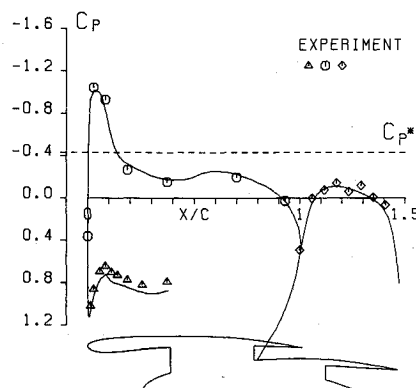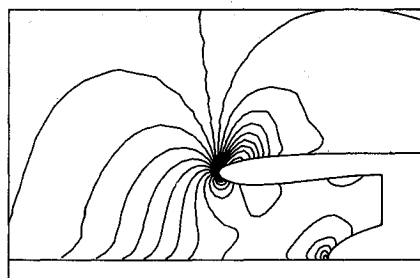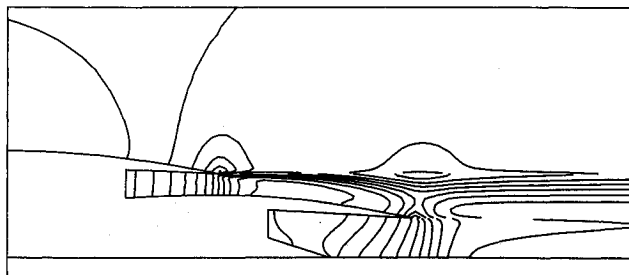

a) Case 13, MFR = 0.31678

b) Case 17, MFR = 0.52324

Fig. 3   Surface pressure distributions on fan cowl and core cowl, $M_\infty = 0.8$.

a) Inlet region

b) Exhaust jet region

Fig. 4   Mach number contours for case 17, $M_\infty = 0.8$.

flow becomes subcritical when MFR is increased. At $M_\infty = 0.7$, the supercritical region expands, and the suction peak remains supercritical even at maximum $MFR = 0.575$. The shock wave is apparent in the computation. At $M_\infty = 0.8$, the supercritical region extends to the 15% chord station, the shock wave remains fixed, and only the suction peak decreases when MFR is changed from minimum to maximum. As MFR is increased, the stagnation point at the leading edge moves outward.

The surface pressure does not recover to the freestream value even at the midchord station. The recovery is obtained behind the 95% chord station. This shows that inclusion of the fan cowl trailing edge is important for the inlet analysis. The flow in the inlet duct is smoothly decelerated, and the mean fan face Mach number agreed well with one-dimensional theory.

The pressure distribution on the core cowl surface also agreed with the experiment. Disagreement at 123% chord station on the core cowl surface as shown in Fig. 3 was due to the improper pressure measurement in the experiment. The distinct lines of the shear layers between the mainflow and fanjet and the fanjet and corejet are captured in Fig. 4b. The fanjet exhaust flow becomes sonic at the nozzle exit, i.e., fan cowl trailing edge in high MFR and high Mach number cases. A supercritical region appears in the exhaust flow along the core cowl surface as shown in Fig. 4b. Resolution of the oblique shock wave pattern, however, was not sufficient because the mesh was not fine enough. Concentration of isobars at the fan cowl and core cowl trailing edge x stations in the mainstream indicates pressure recovery at these regions. These show that the effect of the core cowl trailing edge reaches even to the outer edge of the fanjet stream. Under windmilling conditions, there is no core jet flow, and the fanjet stream expands inward to the x axis in the corejet area. When MFR is increased, the fanjet stream becomes nearly parallel to the x axis.

The corejet flow also becomes sonic at the nozzle exit, i.e., the core cowl trailing edge. A weak diamond shock wave pattern is formed in the stream behind. The corejet flow in the duct is nonuniform in the radial direction as shown in Fig. 4b. A stagnation region appears at the vertex of the plug.

All computed cases gave excellent agreement with the experiment. The present analysis was shown to be valid, and it can be applied to evaluate the effectiveness of a TPS as the real fanjet engine simulation method.

Jet Exhaust Flow at High Power Operation

The last three cases listed in Table 1 show conditions for axisymmetric TPS flow at $M_\infty = 0.8$ with high power operation, and hot jet and real engine flow, respectively. Case 21 is flow with high power operation where pressure and temperature ratios were increased to see their effects. From the pressure contours shown in Fig. 5, pressure distribution along the core cowl surface is not uniform. A pattern of compression and expansion waves are seen in both fanjet and corejet streams. The "external" shear layer between the mainstream and fanjet and the "internal" shear layer between the fanjet and corejet were captured more clearly than the ones obtained in the previous section because of the high pressure and temperature jets. The pressure contours are continuous across
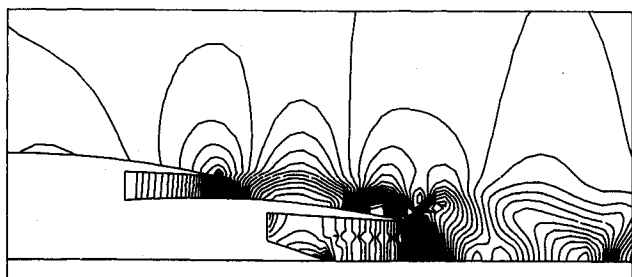
both shear layers, but Mach number and density contours are discontinuous. As just 12 cells were used across each jet width, the resolution in the radial direction was not sufficient to resolve oblique shock waves. An examination of velocity vector plots not shown in the paper, however, shows the wavy flow directions.

Comparison of Cold Jet and Hot Jet

One significant difference between a TPS and a real engine is the corejet temperature. To examine this effect, case 17 for a cold corejet was compared with case 22 for a hot corejet where the corejet temperature ratio (CTR) was increased from 0.61 to 4. Corejet mass flux must be reduced proportionally to $T_0^{-1/2}$ while the jet Mach number and pressure ratio are kept constant. The bypass ratio was increased from 1.57 to 4.01.

Comparison of computed results showed that the pressure distribution on the fan cowl and core cowl surfaces coincided with the cold jet case. The corejet temperature difference did result in significantly different density and velocity distributions in the corejet plume, but the hot corejet effect is attenuated by the surrounding fanjet plume. The main flowfield was not affected because the MFR and fanjet exit conditions were the same with the cold jet case. The present results support the cold corejet simulation used in a TPS with MFR and fanjet

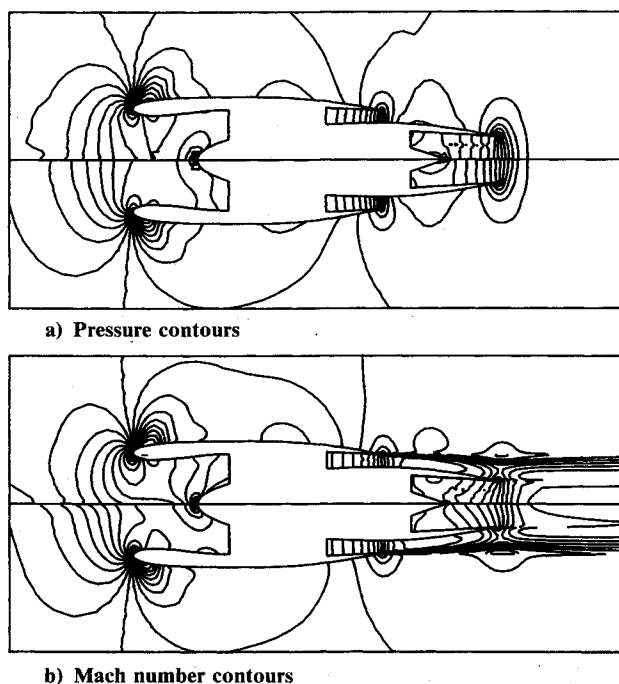a) Pressure contours

b) Mach number contours

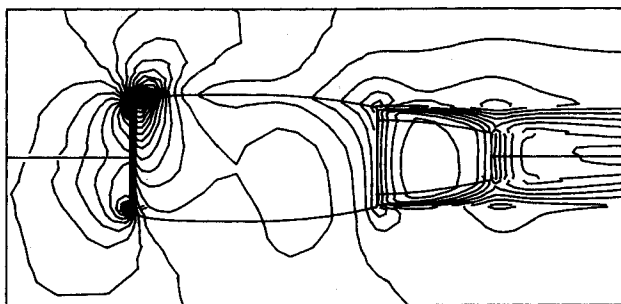Fig. 6   Comparison of contours between real engine (upperhalf) and TPS (lowerhalf) flows.
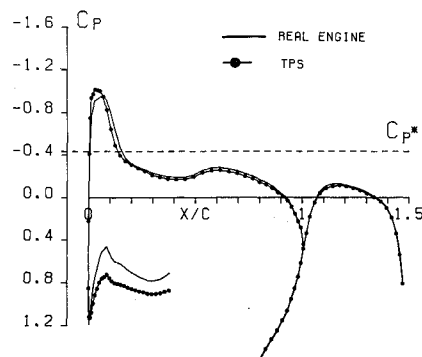
Fig. 7   Comparison of surface pressure distributions on fan cowl and core cowl.
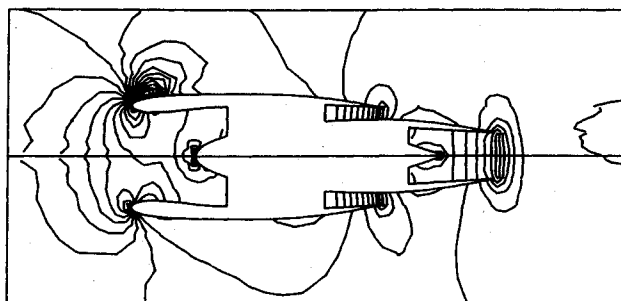
Fig. 5   Pressure contours for high power operation case 21.

a) Pressure contours in symmetry plane

b) Mach number contours on surfaces and in symmetry plane

Fig. 8   Results for three-dimensional flow with coarse mesh, $M_\infty = 0.8$, $\alpha = 9$ deg, $MFR = 0.654$.
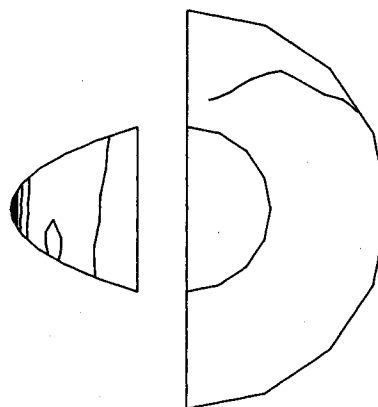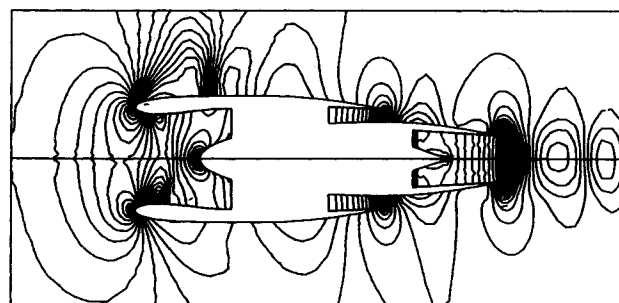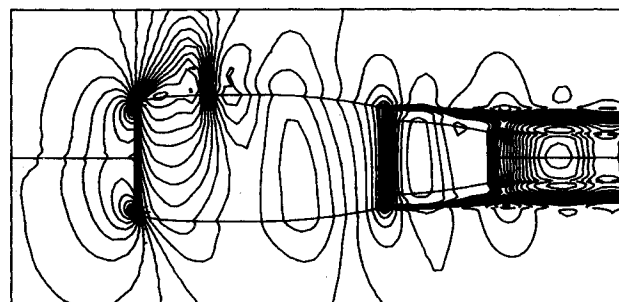

Fig. 9   Pressure contours on fan face and spinner.

a) Pressure contours in symmetry plane

b) Mach number contours on surfaces and in symmetry plane

Fig. 10   Results of fine mesh computation, $M_\infty = 0.9$, $\alpha = 6$ deg, $MFR = 0.8$.

conditions kept the same as in real flight as far as the pressure distribution is concerned.

Comparison of Real Engine and Turbine Power Simulator Flows

The second difference between a TPS and a real engine is the difference of mass flow relations as defined by Eqs. (5) and (6). To examine this effect, the real engine case 23 was computed and compared with the TPS case 17. The fanjet and corejet conditions were the same as for the hot corejet case 22, and MFR was increased to take into account the corejet mass flux.

Figure 6 compares pressure and Mach number contours of the resulting flowfields: upperhalf for the real engine and lowerhalf for the TPS. Figure 7 shows comparison of surface pressure distributions: solid line for the real engine and filled circle for the TPS. The cowl lip shock wave is weaker for the real engine, but the pressure distribution behind the shock wave coincides with the TPS case. The pressure distribution within the inlet duct decreases significantly because of the increase in MFR. The pressure distribution along core cowl surface coincided. The jet flowfield is similar to the hot corejet case. The main flowfield is almost the same as in the TPS case except for the fan cowl lip region. Additional computations at different flow conditions gave similar conclusions.

These results demonstrate that the present code can analyze the major effect of TPS and real engine flows, i.e., the displacement effect of jet mass flux on the mainstream. It can also be said that the TPS testing method simulates the real engine flow condition quite well and predicts the cowl lip shock wave strength on the safe side.

Three-Dimensional Flow of Real Fanjet Engine

Three-dimensional computations simulating the real fanjet engine were made for the following conditions: $M_\infty = 0.8$ and 0.9, angles of attack $\alpha = 0$ to 9 deg, mass flow ratio $MFR = 0.654$ and 0.8. The remaining engine operating conditions were the same as for case 23, the axisymmetric real engine simulation discussed in the previous section. A coarse mesh was used throughout, and each case required 40 min on a FACOM M-780 computer. A fine mesh computation was

made for only one case with $M_\infty = 0.9$ and $\alpha = 6$ deg to check the resolution.

Figure 8a shows pressure contours in the symmetry plane and Fig. 8b shows Mach number contours in the symmetry plane and cowl surfaces at $M_\infty = 0.8$ and $\alpha = 9$ deg. Figure 9 shows pressure contours on the fan face and spinner. The angle of attack effect was well captured in these figures as well as in the rest of the cases, although only 8 cells were distributed in the circumferential direction. The angle-of-attack effect was most significant on the pressure distribution on the fan cowl surface. A cowl lip shock wave stands on the lee side and extends from the symmetry plane to about 45 deg in the azimuthal direction. When the angle of attack is increased, the stagnation point at the cowl lip moves inward, and a supercritical expansion region extends to form a stronger shock wave on the lee side. On the windward side, the opposite phenomenon is observed. Subcritical expansion flow in the windward symmetry plane in the inlet duct increases. The inlet duct flow, which has upwash at the highlight, is rectified to flow along the duct with no crossflow at the fan face. Distortion of the pressure distribution on the fan face is negligibly small in most cases as shown in Fig. 9. The inlet duct flow, however,

becomes supercritical, and a shock wave is formed on the windward side at $\alpha = 9$ deg, $M_\infty = 0.9$, and $MFR = 0.8$. This internal shock wave produces a small amount of nonuniformity.

The downstream flowfield including the jet exhaust plume and the surrounding mainflow behind the midnacelle chord station show a less significant three-dimensional effect at the respective angles of attack. The only exception is that the jet plume is directed parallel to the freestream direction, and development of the mixing shear layer between the fanjet and mainstream differs a little between the lee and windward side. This will be discussed later.

Fine mesh computations are shown in Figs. 10 and 11. Pressure contours are shown in Fig. 10a, and Mach number contours are shown in Fig. 10b. The pressure distribution did not differ significantly from the coarse result, but the resolution was much better. Supercritical regions appeared on the cowl throat for both the windward and lee side in the inlet duct. This was not captured in the coarse mesh analysis. The internal shock wave as well as the cowl lip shock wave are captured more sharply. The jet plume exhibits a diamond shock wave-expansion wave pattern in better resolution even in the far downstream region. The wave length of the pressure wave was the same as the one for the coarse mesh result.

Crossflow velocity vector plots of jet exhaust at several x stations are shown in Fig. 11. The fanjet flow is parallel to the axis without crossflow components at the fan cowl trailing edge, whereas the external mainstream flows along the cowl surface with crossflow components. It is similar to the crossflow past a circular cylinder. Therefore, a shear layer is formed between them and behind the fan cowl trailing edge. The shear becomes apparently most severe at the azimuthal angle of 90 deg. As the flow proceeds downstream, the external flow is entrained into the shear layer. Behind the core cowl trailing edge, the corejet is introduced into the flowfield, and the fanjet-corejet shear layer is formed because the total pressure and total temperature are different. A counter-clockwise vortex appears at $x = 1.8$ in downstream of the jet flow. The engine body and jet exhaust plume constitute an "effective solid cylinder" at angle of attack, and the present flow resembles such a flow with a pair of separating vortices. The corejet receives upwash and it is turned upward.

In the present analysis, mixing in the shear layer is provided by numerical dissipation terms. The coefficient of dissipative terms in the azimuthal direction was kept to a minimum so that its effect is less significant. The capturing of vortical flow in an

Euler analysis is well known. A typical example is flow past a delta wing at large angle of attack.[33] Although the present analysis uses third-order dissipation, the mesh size is not fine enough. This causes relatively large numerical dissipation in the solution. Since coarse mesh and fine mesh solutions are in good agreement, it can be said that the solution gives qualitatively the appearance of a vortical flowfield in the jet exhaust flow, and the result can be interpreted as an approximate low Reynolds number flow. Use of a much finer mesh will provide a sharper shear layer solution. It should also be noted that a Navier-Stokes code with a coarse mesh does not provide quantitatively good viscous solutions unless the cell-Reynolds number is of the order of unity. Most of the previous works neglect this point and "numerically low Reynolds number" flow has been presented. The investigation of more details is not in the scope of the present work and must be addressed in the future.

Conclusion

Axisymmetric and three-dimensional Euler analysis of a TPS and fanjet engine was made. Results were compared with experimental data for a TPS in transonic flow. Surface pressure distributions on the fan cowl and core cowl showed excellent agreement with experiment. The evaluation of differences between a TPS and real engine was presented. The main flowfield surrounding the exhaust jet plume was almost the same in both cases except for the fan cowl lip region. This supports the validity of the TPS testing method in simulating engine effects in wind tunnel testing. Angle of attack effects on the inlet flow and jet exhaust plume were obtained in a three-dimensional real engine analysis. The computed flowfield for jet plume shear layer showed vortical flow. Detailed discussion of Euler vortical flow and viscous effects will be areas of future research.

References

[1]Bagley, J. A., and Kurn, A. G., "Jet Interference on Super-critical Wings," ARC R&M No. 3845, 1977.

[2]Langley, M. J., "The Design of Axisymmetric Cowls for Podded Nacelles for High By-pass Ratio Turbofan Engines," ARC R&M No. 3846, 1979.

[3]Crook, J. L., Nelson, D. P., Wiley, R. H., and Presz, W. M., "Isolated Nacelle Performance-Measurement and Simulation," AIAA Paper 82-0134, 1982.

[4]Asai, K., Suzuki, K., Hagii, K., Nakamura, M., Suenaga, N., and Hosoe, N., "Power Effects on Transonic Characteristics of USB-STOL Aircraft—A Transonic Wind Tunnel Experiment Result," Proceedings of 1987 Aircraft Symposium, Japan Society for Aeronautical and Space Sciences, Oct. 1987, pp. 258–261.

[5]Asai, K., Nakamura, M., Koike, A., Suzuki, K., Oguni, Y., Karasawa, T., Noto, T., and Hoshi, K., "Construction of Turbine-Powered Model Testing System in the Transonic Wind Tunnel," Proceedings of 1986 Annual Meeting, Japan Society for Aeronautical and Space Sciences, April 1986, pp. 153–156.

[6]Koike, A., Asai, K., Hosoe, N., Karasawa, T., Suenaga, N., Mitsuhori, S., and Suzuki, K., "Transonic Operational Characteristics and Performance of Two Turbine-Powered Simulators Determined from Wind Tunnel Tests," National Aerospace Lab., Chofu, Japan, TR-968, 1988.

[7]Arlinger, B. G., "Calculation of Transonic Flow around Axisymmetric Inlets," AIAA Journal, Vol. 13, No. 12, 1975, pp. 1614–1621.

[8]Caughey, D. A., and Jameson, A., "Accelerated Iterative Calculation of Transonic Nacelle Flowfields," AIAA Journal, Vol. 15, No. 10, 1977, pp. 1474–1480.

[9]Chen, L. T., and Caughey, D. A., "Calculation of Transonic Inlet Flowfields Using Generalized Coordinates," Journal of Aircraft, Vol. 17, No. 3, 1980, pp. 167–174.

[10]Chen, L. T., and Caughey, D. A., "Higher Order, Finite-Difference Scheme for Three Dimensional Transonic Flowfields about Axisymmetric Bodies," Journal of Aircraft, Vol. 17, No. 9, 1980, pp. 668–676.

[11]Reyhner, T. A., "Transonic Potential Flow Computation about Three-Dimensional Inlets, Ducts, and Bodies," AIAA Journal, Vol. 19, No. 9, 1981, pp. 1112–1121.

[12]Vadyak, J., and Atta, E. H., "Approximate Factorization Algorithm for Three-Dimensional Transonic Nacelle/Inlet Flowfield
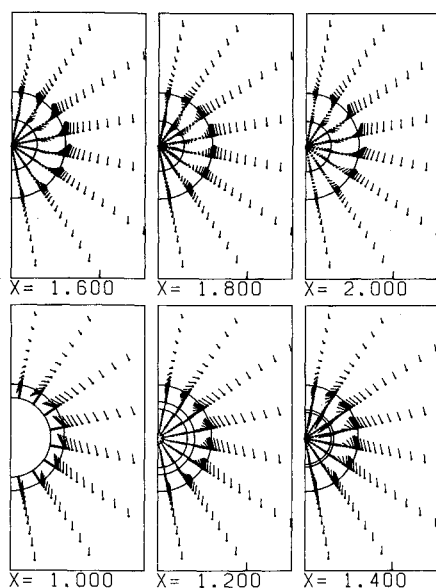
Fig. 11　Crossflow velocity vectors at several x stations.

Computations," *Journal of Propulsion and Power*, Vol. 1, No. 1, 1985, pp. 58–64.

[13]Nakamura, T., "Numerical Computation of Transonic Potential Flow about Three-Dimensional Inlets," National Aerospace Lab., Chofu, Japan, TR-924, 1987.

[14]Peace, A. J., "Transonic Flow Calculations around Isolated Inlet Configurations," AIAA Paper 85-1596, 1985; see also *Aeronautical Journal*, March 1986, pp. 103–110.

[15]Morice, P., Cambier, L., and Veuillot, J. P., "Numerical Computation of Transonic Flow Past an Axisymmetric Nacelle," ICAS Paper 84-1.10.2, 1984.

[16]Deese, J. E., and Agarwal, R. K., "Calculation of Axisymmetric Inlet Flowfield Using the Euler Equations," AIAA Paper 83-1853, 1983.

[17]Chen, H. C., Yu, N. J., and Rubbert, P. E., "Flow Simulations for General Nacelle Configurations Using Euler Equations," AIAA Paper 83-0539, 1983.

[18]Chen, H. C., Kusunose, K., and Yu, N. J., "Flow Simulations for Detailed Nacelle-Exhaust Flow Using Euler Equations," AIAA Paper 85-5003, 1985.

[19]Nakahashi, K., and Obayashi, S., "FDM-FEM Zonal Method for Viscous Flow Computations over Multiple-Bodies," National Aerospace Lab., Chofu, Japan, TR-925T, 1987; see also AIAA Paper 87-0604, 1987.

[20]Rubbert, P. E., "The Emergence of Advanced Computational Methods in the Aerodynamic Design of Commercial Transport Aircraft," *Preprints of Vol. II of International Symposium on Computational Fluid Dyanmics—Tokyo*, Sept. 9–12, 1985.

[21]Bowers, D., and Laughrey, J., "A Summary of an AGARD Assessment of Testing Techniques for Aircraft Afterbody Flows," AIAA Paper 85-1465, 1985.

[22]Putnam, L. E., and Bissinger, N. C., "Results of AGARD Assessment of Prediction Capabilities for Nozzle Afterbody Flows," AIAA Paper 85-1464, 1985

[23]Peery, K. M., and Forester, C. K., "Numerical Simulation of Multistream Nozzle Flows," *AIAA Journal*, Vol. 18, No. 9, 1980, pp. 1088–1093.

[24]Deiwert, G. S., and Rothmund, H., "Three Dimensional Flow over a Conical Afterbody Containing a Centered Propulsive Jet: A Numerical Simulation," AIAA Paper 83-1709, 1983.

[25]Hirose, N., and Kawamura, R., "Numerical Calculation of Supersonic Opposing Jet Directed Upstream against Supersonic Main Stream by the Use of Time-Dependent Finite-Difference Method," *Proceedings of the 9th International Symposium on Space Technology and Science, Tokyo 1971*, 1971, pp. 311–317.

[26]Yee, H. C., and Shin, J. L., "Semi-Implicit and Fully Implicit Shock-Capturing Methods for Hyperbolic Conservation Laws with Stiff Source Terms," AIAA Paper 87-1116, 1987.

[27]MacCormack, R. W., "The Effect of Viscosity in Hypervelocity Impact Cratering," AIAA Paper 69-354, 1969.

[28]Rizzi, A., and Inouye, M., "Time-Spilt Finite-Volume Method for Three-Dimensional Blunt-Body Flow," *AIAA Journal*, Vol. 11, No. 11, 1973, pp. 1478–1485.

[29]Tani, T., Arai, N., Takehana, K., Sekine, H., and Hirose, N., "Subsonic Flow Region on Blunted Cones in Supersonic Flow," *Journal of the Japan Society for Aeronautical and Space Sciences*, Vol. 35, May 1987, pp. 253–259.

[30]Hirose, N., Takanashi, S., Sekigami, S., and Kawamura, R., "Cascade Design Procedure Utilizing Inverse Cascade Method and 2-D Euler Analysis Code," *Proceedings of 1988 Fluiddynamics Conference*, Japan Society for Aeronautical and Space Sciences, Nov. 1988, pp. 58–61.

[31]Jamesson, A., and Baker, T. J., "Solution of the Euler Equations for Complex Configurations," AIAA Paper 83-1929, 1983.

[32]Hirose, N., Asai, K., and Ikawa, K., "Transonic 3-D Euler Analysis of Flows around Fanjet Engine and T. P. S.," National Aerospace Lab., Chofu, Japan, TR-1045 (to be published).

[33]Murman, E. M., "Transonic Vortical Flow," *Symposium Transsonicum III*, edited by J. Zierep and H. Oertel, Springer-Verlag, Berlin, 1988, pp. 265–279.